water

MDPI

Article

Investigating Arctic Permafrost Dynamics Using Electrical Resistivity Imaging and Borehole Measurement in Svalbard

Ding-Jiun Lin [1], Ping-Yu Chang [1,2,*], Ying-Lon Chen [1], Jordi Mahardika Puntu [1], Chuen-Fa Ni [1,3,4], Slawomir Jack Giletycz [1,3], Ireneusz Sobota [5], Kamil Czarnecki [5] and Yu-Huan Chang [4]

1 Department of Earth Sciences, National Central University, Taoyuan 330, Taiwan; jim325462@g.ncu.edu.tw (D.-J.L.)
2 Earthquake Disaster & Risk Evaluation and Management Center (E-DREaM), National Central University, Taoyuan 330, Taiwan
3 Taiwan Polar Institute, National Central University, Taoyuan 330, Taiwan
4 Graduate Institute of Applied Geology, National Central University, Taoyuan 330, Taiwan
5 Department of Hydrology, Cryology and Water Management, Nicolaus Copernicus University in Toruń, 87-100 Toruń, Poland
* Correspondence: pingyuc@ncu.edu.tw

Abstract: This study utilized electrical resistivity imaging (ERI) to investigate subsurface characteristics near Nicolaus Copernicus University Polar Station on the western Spitsbergen-Kaffiøyra Plain island in the Svalbard archipelago. Surveys along two lines, LN (148 m) collected in 2022 and 2023, and ST (40 m) collected in 2023, were conducted to assess resistivity and its correlation with ground temperatures. The LN line revealed a 1- to 2-m-thick resistive unsaturated outwash sediment layer, potentially indicative of permafrost. Comparing the LN resistivity result between 2022 and 2023, a 600 Ohm.m decrease in the unsaturated active layer in 2023 was observed, attributed to a 5.8 °C temperature increase, suggesting a link to global warming. ERI along the ST line depicted resistivity, reaching its minimum at approximately 1.6 m, rising to over 200 Ohm.m at 4 m, and slightly decreasing to around 150 Ohm.m at 7 m. Temperature measurements from the ST line's monitoring strongly confirmed that the active layer extends to around 1.6 m, with permafrost located at greater depths. Additionally, water content distribution in the ST line was estimated after temperature correction, revealing a groundwater depth of approximately 1.06 m, consistent with measurements from the S4 borehole on the ST line. This study provides valuable insights into Arctic subsurface dynamics, emphasizing the sensitivity of resistivity patterns to climate change and offering a comprehensive understanding of permafrost behavior in the region.

Keywords: electrical resistivity imaging; borehole temperature; permafrost; Svalbard; groundwater; active layer

Citation: Lin, D.-J.; Chang, P.-Y.; Chen, Y.-L.; Puntu, J.M.; Ni, C.-F.; Giletycz, S.J.; Sobota, I.; Czarnecki, K.; Chang, Y.-H. Investigating Arctic Permafrost Dynamics Using Electrical Resistivity Imaging and Borehole Measurement in Svalbard. *Water* **2024**, *16*, 2707. https://doi.org/10.3390/w16192707

Academic Editors: Alex Sendros, María del Carmen Cabrera Santana and Albert Casas Ponsati

Received: 6 August 2024
Revised: 12 September 2024
Accepted: 15 September 2024
Published: 24 September 2024

1. Introduction

Permafrost, characterized by ground where temperature remains below 0 °C for at least two consecutive years [1,2], covers approximately one quarter of the land area in the Northern Hemisphere [3–5]. The thermal state of permafrost is highly sensitive to changes, primarily due to climate conditions [1,6,7]. Arctic warming amplification, a well-established phenomenon with Arctic warming approximately twice as fast as the global average, is altering the distribution of permafrost worldwide and causing its decline [7–9]. The top layer of soil above the permafrost is subject to seasonal thawing and freezing, the so-called Active Layer. Frequent thawing and freezing caused by climate warming will increase the Active Layer Thickness (ALT) and lead to a general reduction in surface permafrost area. This seasonal thawing and freezing of the active layer will shrink and expand due to the contraction and expansion of pore water, which will cause thawing and settlement, reduce foundation stress and ground bearing capacity, and lead to infrastructure deformation [10].

As permafrost thawing intensifies, an observable increase in ALT is noted across permafrost regions, reflecting ongoing climate change impacts [11–15]. The phenomena might become more rapid in the future, and thawing permafrost could also impact local construction (Figure 1). Therefore, monitoring permafrost variation becomes crucial. However, it is challenging to determine and monitor active layer conditions through direct excavation, core drilling, or the installation of downhole temperature sensors. Consequently, indirect geophysical surveys, such as Electrical Resistivity Imaging (ERI) and Ground Penetrating Radar (GPR), are often employed for regional ALT investigation, providing near-surface indicators of subsurface soil conditions [16–18]. In our study, we conducted an ERI survey at the Kaffiøyra Plain, near the Nicholas Copernicus University Polar Station (NCUPS) during the summers of 2022 and 2023. The 185-m-long survey line extends from the research station to the coastline, allowing us to monitor and analyze changes in the permafrost and active layers influenced by global warming.

Figure 1. The impact of the thawing permafrost on construction in Svalbard. (**a**) Warehouse damaged, and (**b**) slanted house foundation due to permafrost thawing.

2. Study Site and Survey Configuration

Our study area was located at the Kaffiøyra Plain near the Nicolaus Copernicus University Polar Station (NCUPS) on the western Spitsbergen Island of Svalbard archipelago, Norway (Figure 2). Kaffiøyra is a coastal plain located in north-western Spitsbergen (Oscar II Land), and constitutes the largest island of the Svalbard archipelago. It covers an area of 2582 km^2, 70% of which is represented by glaciers, stretching across nearly 1600 km^2. The glacierized areas predominantly comprise ice plateau, from which glaciers emanate [19]. The majority of Kaffiøyra terrain is covered by moraines and tundra, consisting of outwash from the adjacent glaciers. The NCUPS is situated in the northern part of the Kaffiøyra, adjacent to Hornbreak bay, formed by the retreating Avatsmarkbreen. Near the NCUPS, the river system is primarily contributed to by a smaller glacier, Waldemarbreen, which is located south of the large glacier bordering the Kaffiøyra Plain to the north, the Aavatsmarkbreen (Figure 2). The recession of the glaciers in the Kaffiøyra area during the analytical period is attributed to a negative trend in the mass balance and dynamics of the Svalbard glaciers [20,21]. Consequently, the dry creek bed of the Waldemarbreen river system is observed near the NCUPS. The air temperature displayed a statistically significant upward trend of 0.28 °C·10 yr^{-1} during the summer expedition period (21 July–31 August) from 1975 to 2017. Since the beginning of the measurements, the temperature has risen by 1.4 °C [22]. Temperature also impacts the active layer above the permafrost; compared to the period between 1996 and 2012, the average thickness of the active layer in the Kaffiøyra region increased by 3% (tundra), 5% (glacier moraine), and 6% (beach) from 2008 to 2012.

The ERI survey was conducted near the beach, where the geological structure primarily consists of sand and gravelly sand characterized by horizontal and low-angle cross-bedding. These sediments exhibit sorting that ranges from very poor to moderately well sorted, with median grain diameters between 0.25 and 0.88 mm. The lithological details are based on previous research by Sobota and Nowak [12].

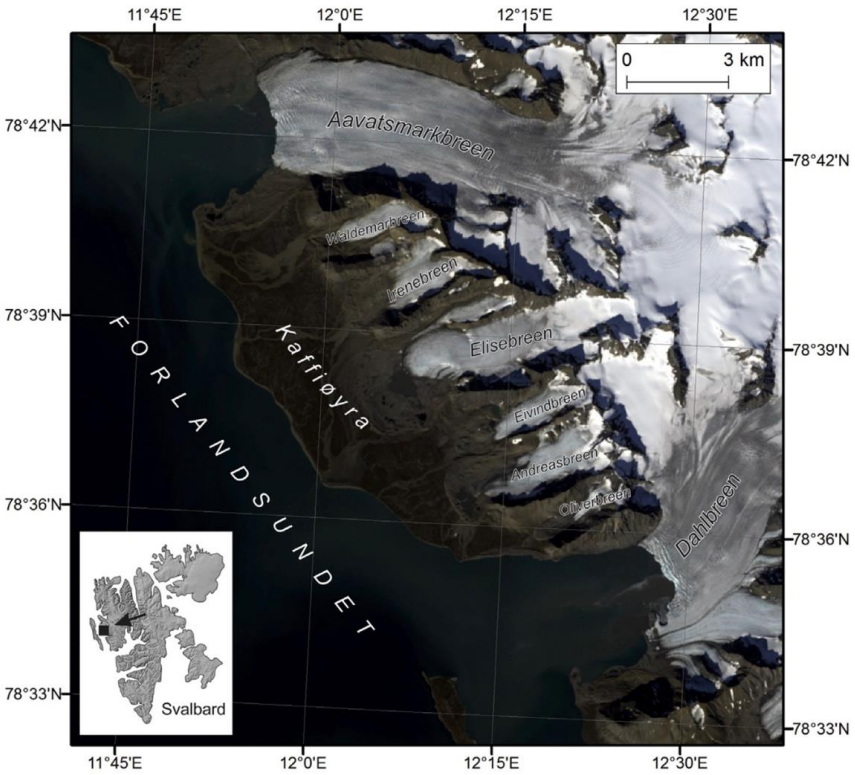

Figure 2. The location of the Kaffiøyra Plain and the adjacent glaciers in north-western Spitsbergen, Norway [20].

We conducted the ERI survey along the LN line (Figure 3) in August of 2022 and 2023. The LN line is about 148 m long, with direction perpendicular to the coastline and, along the LN line, we drilled five shallow boreholes, namely S1, S2, S3, S4, and S5 (see Table 1), to monitor the groundwater levels and temperatures, which are measured at hourly intervals. On the other hand, a new borehole equipped with temperature sensors was installed near the weather station, as shown in Figure 3. We conducted an ERI survey along the 40-m-long ST line in order to compare measured resistivity with subsurface temperatures.

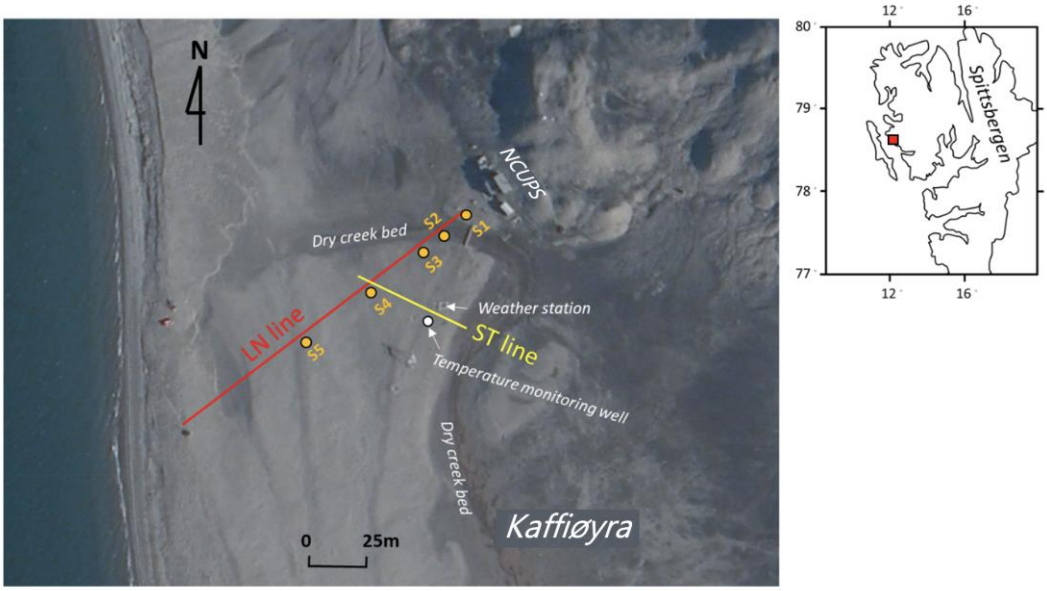

Figure 3. The survey design at the NCUPS on Kaffiøyra located on the Spitsbergen island of the Svalbard archipelago. The red box represents the location of NCUPS.

Table 1. The locations and configurations for the observation boreholes at the study site.

Borehole No.	Coordinate-X	Coordinate-Y	Ground Elevation (m)	Pressure Sensor Elevation (m)
S1	8,735,652.0	430,441.6	1.463	0.573
S2	8,735,658.5	430,449.6	1.861	1.391
S3	8,735,608.0	430,386.9	2.831	1.941
S4	8,735,627.2	430,410.4	2.160	0.880
S5	8,735,645.9	430,433.6	1.858	0.668

The field data measurements were conducted using a 4-point light 10W resistivity meter and a multiple active electrode (ActEle) system [23]. In August 2022, we utilized 20 ActEle electrodes in a roll-along configuration to collect data along the profile. In order to achieve greater exploration depth, we increased the number of electrodes to 40 in the August 2023 survey. We applied the Wenner (WN) array with 1-m electrode spacing for the ERI surveys, as higher signal-to-noise ratios and greater sensitivity to horizontal structures are frequently obtained with the WN array [24], such as variation in groundwater tables [25,26]. Additionally, the average contact resistance of each electrode was 7.767 kΩ, with a maximum value of 15.865 kΩ. A few data points were affected by high-contact resistance, leading to larger measurement errors. The anomalous data were removed during the subsequent inversion process, as shown in Figure 4. We used the software EarthImager2D^{TM} [27], a two-dimensional (2D) inversion program developed by Advanced Geosciences Inc., AGI, Austin, TX, USA. EarthImager2D^{TM} facilitates the computation of the optimum resistivity models by utilizing an iterative conjugate gradient inversion method and finite-element forward solutions [28]. A comprehensive review of inversion method for resistivity studies can be found in Sharma and Verma [29].

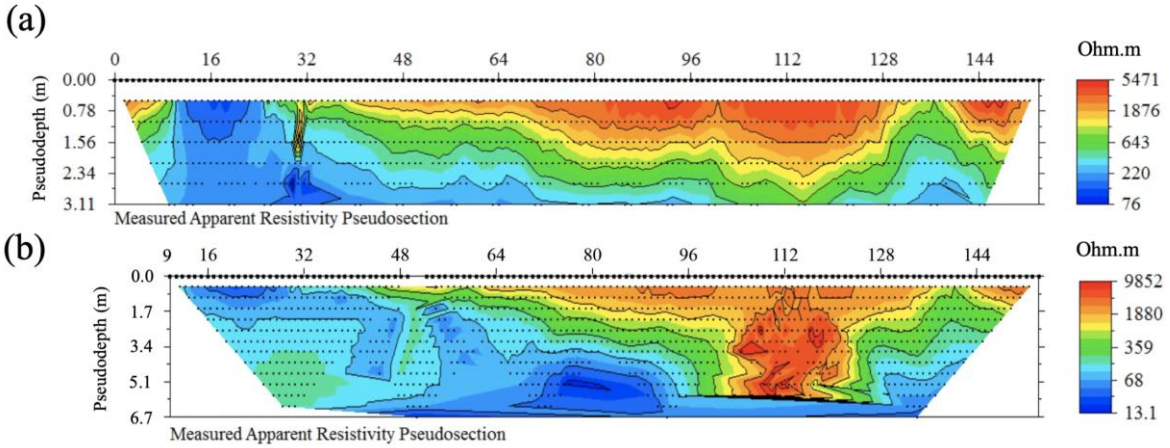

Figure 4. (**a**) Measured apparent resistivity pseudo-section of LN line in (**a**) 2022 and (**b**) 2023; the points represent each measured data point with the roll-along measurement.

3. Results

Figure 5a displays the inverted resistivity images of the LN line collected in 2022. Boreholes S1, S2, S3, S4, and S5 are located at 9 m, 19 m, 29 m, 59 m, and 89 m along the LN survey line. In August 2022, we observed that the near-surface regions consist mainly of resistive materials with resistivity values exceeding 2000 Ohm.m, spanning from 0 to 9 m and 33 to 158 m along the LN line. These resistive regions correspond to unsaturated outwash sediments, with a thickness of the resistive region ranging from 1 to 2 m. Below the surface resistive layer, the resistivity rapidly decreased to less than 500 Ohm.m, which may indicate the presence of the permafrost layer. Between 13 and 24 m along the LN line, the near-surface region exhibited resistivity of less than 100 Ohm.m, indicating the possibility of perched groundwater beneath the dried creek bed. Some conductive structures extending

deeper from the shallow perched groundwater may suggest vertical infiltration paths through the talik in the permafrost.

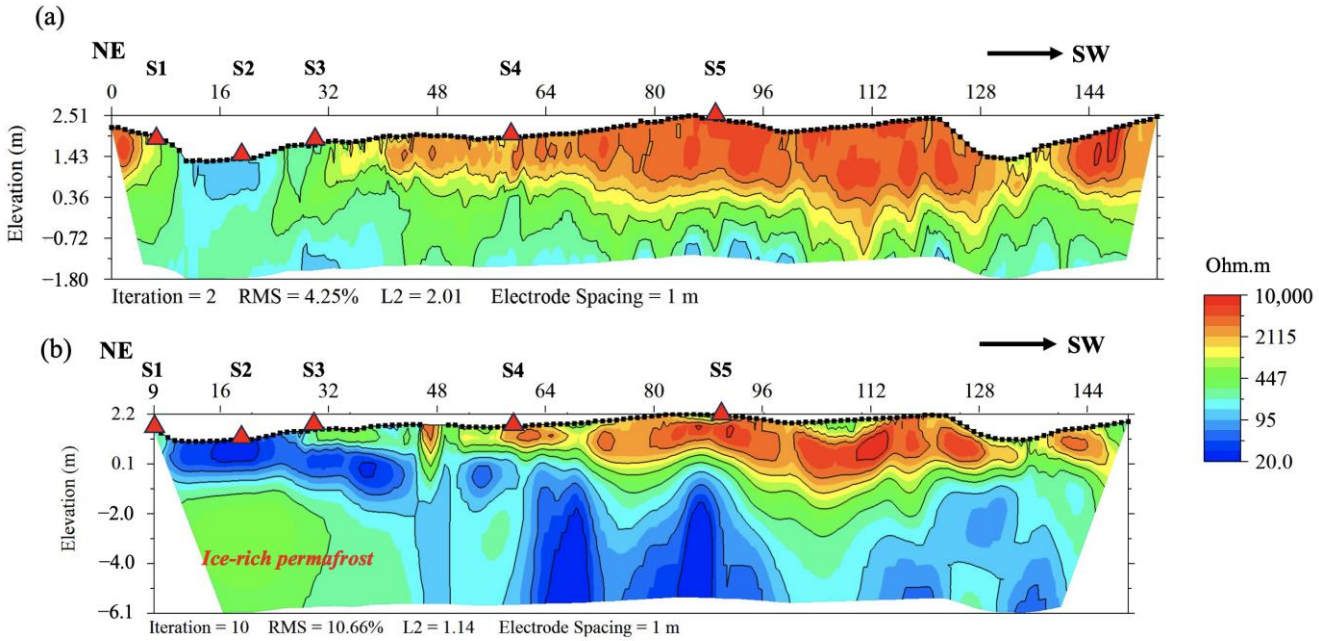

Figure 5. (**a**) The inverted resistivity image of the LN line collected in 2022. (**b**) The inverted resistivity image of the LN line collected in August 2023. The blank areas indicate measurements that were deleted due to poor electrode coupling. The observation boreholes are represented as red triangles with S1, S2, S3, S4, and S5.

Figure 5b displays the resistivity images of the LN line collected in 2023. The survey originates from the location of the S1 borehole, designated as 9 m in the 2023 surveys, due to the loss of the original starting marker. Owing to poor electrode contact, measurements from four electrodes had to be excluded, resulting in blank areas in the inverted results beneath these electrodes. Similar to the result in 2022, we identified a resistive unsaturated layer extending from 55 to 148 m along the LN line, with a thickness ranging from 1 to 2 m. Below this unsaturated layer, the resistivity decreased to mostly less than 500 Ohm.m between 0 and 60 m on the LN line, indicative of the permafrost layer. However, the region beneath the unsaturated sediments exhibited resistivity values of less than 100 Ohm.m between 0 and 60 m on the LN line.

The low resistivity values might be influenced by three factors. First, the distribution of melting talik and groundwater conduits due to the thermokarst effect. Second, the proximity to the coastline may lead to seawater intrusion, affecting resistivity. Third, the lithological variations might be influenced by the release of ions from sediments. However, the second and third factors may not be the primary influences. The lithology of the study area primarily consists of sand and gravelly sand characterized by horizontal and low-angle cross-bedding [13]. If seawater intrusion were significant, the resistivity on the coastal side (profile distance over 112 m) should be lower than on the side near the NCU station, which is closer to the moraine and dry creek bed. However, the low resistivity is observed near the station.

Therefore, we consider the main cause of the low resistivity along the LN line, particularly between 13 and 60 m beneath the dry creek bed, to be the distribution of melting talik and groundwater conduits resulting from the thermokarst effect. This could allow water to percolate downward and connect horizontally to the channel, which may be underlain by potentially resistive, ice-rich permafrost.

Compared to the measured groundwater table during the same period in 2022 and 2023, it is evident that the groundwater table appeared to be shallower in wells S2 and S3, which were located in the dry creek bed, and deeper in wells S1, S4, and S5 (Table 2).

Additionally, the groundwater table was roughly consistent with the 400-Ohm.m boundary between the resistive shallow ground and the conductive subsurface.

Table 2. The average groundwater table measured during the monitoring periods in 2022 and 2023.

Borehole No.	2022 Avg. Groundwater Depth (m) *	2022 Groundwater Table Elevation (m)	2023 Avg. Groundwater Depth (m) +	2023 Groundwater Table Elevation (m) +
S1	0.779	0.684	N.A. #	N.A. #
S2	0.403	1.458	0.126	1.735
S3	0.830	2.001	0.799	2.032
S4	1.287	0.873	1.295	0.865
S5	1.220	0.638	1.219	0.639

Notes: * during 16 August to 22 August 2022, + during 11 August to 17 August 2023, # sensor malfunction.

In August 2023, a new monitoring well, equipped with temperature sensor arrays, was completed. To compare the temperature measurements with the resistivity data, we drew the ST line, which extended from the area near the S4 borehole to the weather station. Figure 6 displays the inverted electrical resistivity image of the ST survey line. The upper 1–2 m consisted of unsaturated resistive sediments with resistivity higher than 1000 Ohm.m. Below the unsaturated sediments lay a conductive layer with resistivity of less than 200 Ohm.m, which may indicate possible groundwater above the permafrost layer. Further below the conductive layer, the resistivity increased to approximately 200–600 Ohm.m in the region between 5 and 27 m on the ST line, suggesting the presence of frozen permafrost. In addition to the permafrost region, the areas between 0 and 4 m, and between 28 and 39 m, mainly consisted of low-resistivity materials with resistivity of less than 150 Ohm.m, indicating the possible presence of a melting talik.

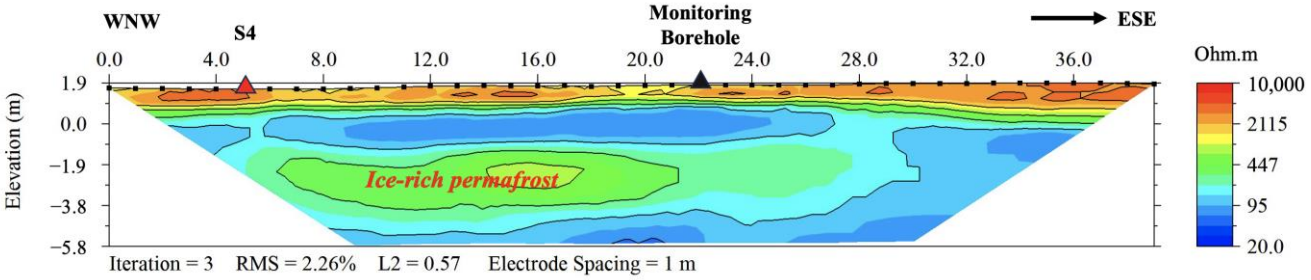

Figure 6. The inverted resistivity image of the ST line collected in 2023. S4 is the observation borehole and also the cross point with the LN line. Monitoring well is represent as black triangle. The observation boreholes are represented as red triangles with S4.

Figure 7 shows the downhole temperature measured in the borehole temperature monitoring well alongside the vertical resistivity extracted from the resistivity model of the SN line near the well. Generally, the temperature between 2 m and 8 m deep mainly ranged from 0 to −2 °C. Additionally, we observed that the soil above a depth of 2 m was above 0 °C, with resistivity reaching a low value of about 50 Ohm.m at a depth of 1.8 m.

These temperature measurements confirm the existence of a deeper permafrost level below 2 m. Furthermore, we observed inconsistent trends between the vertical temperature and resistivity. Specifically, the resistivity reached its lowest at a depth of about 1.6 m, then increased to over 200 Ohm.m at about 4 m, and slightly decreased to around 150 Ohm.m at a depth of 7 m. However, the temperature quickly decreased from 6 °C at the ground surface to 0 °C at about 2 m deep. The temperature remained between 0 and −2 °C at 2 to 5 m deep, gradually decreasing to lower than −1 °C at a depth of 7 m. This observation may imply the existence of resistive ice-rich permafrost between 2 m and 5 m deep in the ST line.

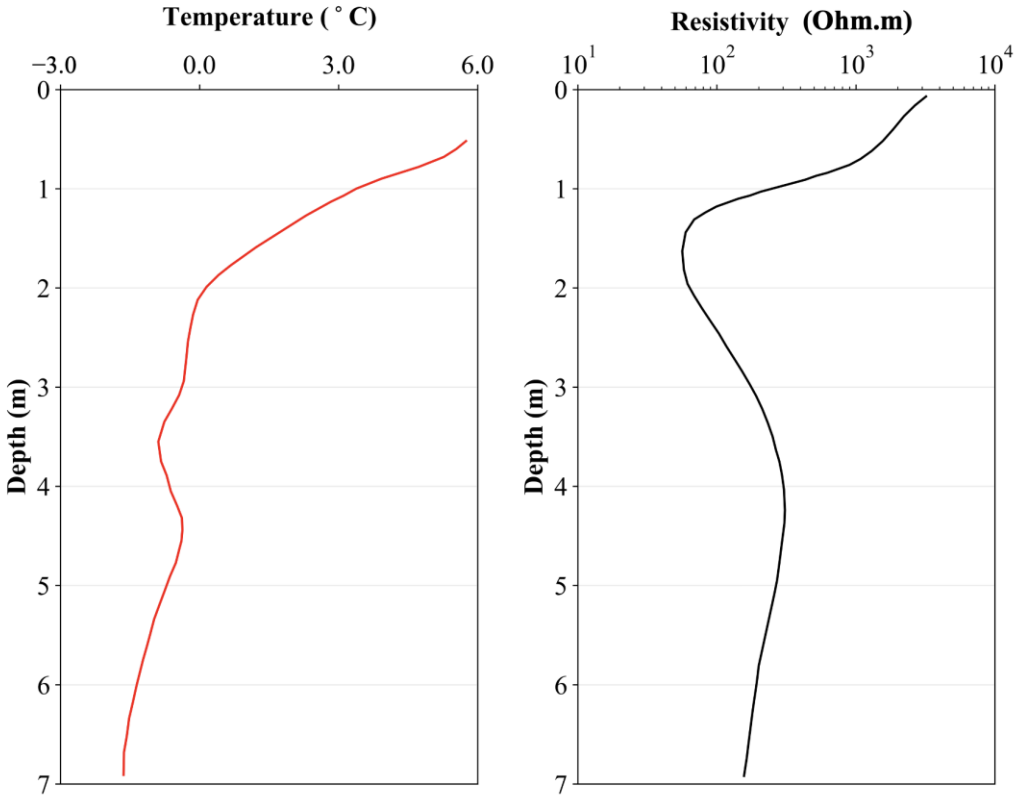

Figure 7. (**Left**): Temperature measured in the monitoring well. (**Right**): Vertical resistivity profile from the ST line at the monitoring borehole location.

4. Discussion

4.1. Resistivity Difference between 2022 and 2023

Figure 8 illustrates the differences in inverted resistivity between August 2022 and August 2023. Svalbard experienced average temperatures of 2.5 °C and 8.3 °C in August during the measuring periods of 2022 and 2023, respectively (https://www.yr.no/en/statistics/table/5-99910/Norway/Svalbard/Svalbard, accessed on 15 July 2024). Several physical factors may affect the measured subsurface resistivity, including lithology, mineral composition, water content, porosity, pore structure and connectivity, and pore water composition [30], along with temperature variations [31]. Since there was no precipitation during the measuring periods in both 2022 and 2023, the temperature increase of 5.8 °C resulted in a significant decrease of several hundred Ohm.m in resistivity in the active layer near the surface.

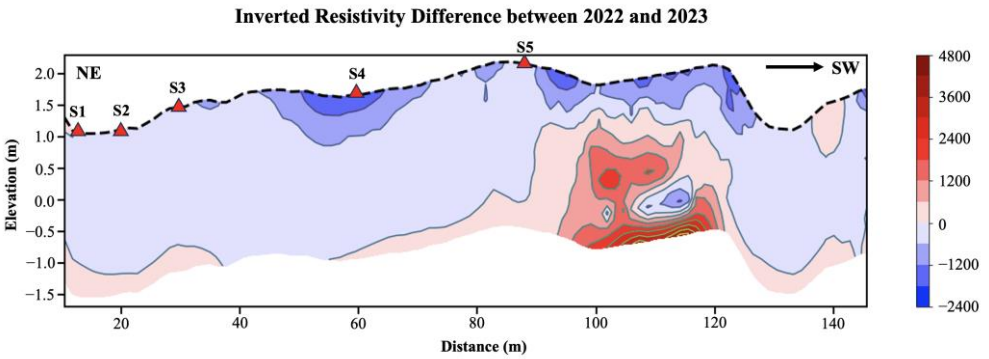

Figure 8. The resistivity difference between measurements taken in August 2022 and 2023. The observation boreholes are represented as red triangles with S1, S2, S3, S4, and S5.

Additionally, we observed a region with increased resistivity exceeding 1200 Ohm.m between 90 and 120 m along the survey line at depths of 0.5–3 m in the LN profile. This higher resistivity may indicate the presence of remaining ice wedges in the active layer, as ice typically exhibits higher resistivity compared to unfrozen soils.

4.2. The Variation of the Active Layer and Permafroste

Permafrost is defined as ground that remains at or below 0 °C for at least two consecutive years. Based on the temperature and resistivity data shown in Figure 7, it can be concluded that at depths shallower than 2 m, the temperature consistently remained above 0 °C, with resistivity reaching its lowest point at around 1.6 m. Therefore, it can be inferred that no permafrost was present above this depth on the beach of Kaffiøyra.

The surface layer in this area consisted of unsaturated, poorly sorted sand and gravel [12,13]. We compared the long-term monitoring data on the maximum thickness of the active layer in the Kaffiøyra plain from 1996 to 2015. The trend coefficient for active layer thickness change on the beach was estimated to be +1.284 (±0.378) cm per year, with a thickness of 117 cm in 1996 [13]. Based on this trend, the active layer thickness in 2023 was estimated to be approximately 1.53 (±0.1) meters, which aligns with the lowest resistivity observed at around 1.60 m. The increase in active layer thickness might relate to rising temperatures, which contribute to permafrost thawing and the melting of talik, as shown in Figure 9. This temperature rise accelerates permafrost degradation, leading to a deeper active layer over time. Thus, we suggest that the active layer extends to around 1.6 m, with permafrost located at greater depths.

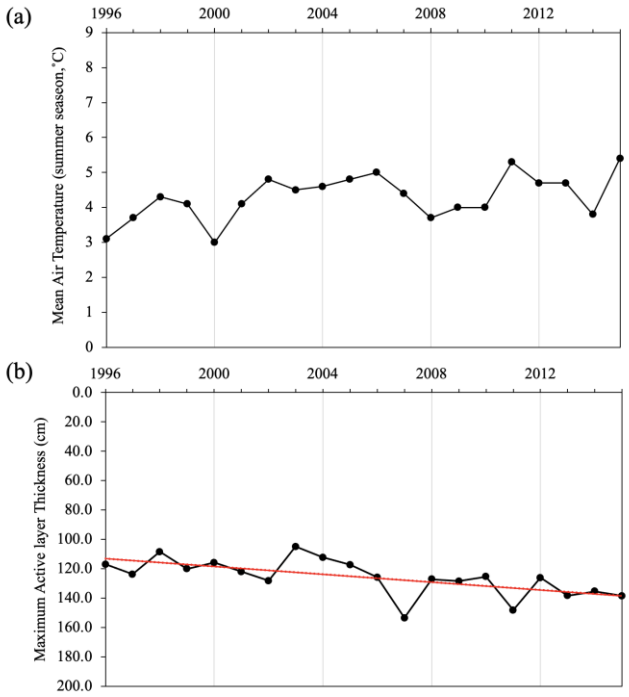

Figure 9. Variation in temperature and active layer thickness: (**a**) mean summer air temperature in Ny-Ålesund from 1996 to 2023; (**b**) maximum active layer thickness on the beach of Kaffiøyra from 1996 to 2015, with the red line representing the trend line (based on Sobota et al. [13]).

4.3. Determining Hydraulic Parameters within the Active Layer

In the active layer above the permafrost, soil and rock resistivity is influenced by the resistivity of pore fluid, porosity, as well as saturation and cementation status. According to Archie's law [30,32], an empirical formula to describe the relationships between the

bulk resistivity of soils/rocks (ρ_b), porosity (ϕ), saturation (S_w), and resistivity of pore water (ρ_w):

$$\rho_b = \alpha \rho_w \phi^{-m} {S_w}^{-n}, \tag{1}$$

where α is the tortuosity factor, and n and m are the saturation index and cementation index, respectively. The resistivity of pore water was 804 µS/cm from the in situ borehole measurement. In general, for homogeneous rocks and soils, m ranged from 1.8 to 2.2, and the value of n was about 2, thus, considering $m = n \cong 2$, Equation (1) is approximated as:

$$\rho_b = \alpha \rho_w \theta^{-2}, \tag{2}$$

where θ is the volumetric water content. The relationship between the unsaturated and saturated zones can be expressed as:

$$\frac{\rho_u}{\rho_s} = \frac{\alpha \rho_w {\theta_u}^{-2}}{\alpha \rho_w {\theta_s}^{-2}} \tag{3}$$

where θ_u and ρ_u represent the volumetric water content and resistivity in the unsaturated zone; θ_s and ρ_s represent the volumetric water content and resistivity in the saturated zone.

According to Table 1, the groundwater table is at a depth of 1.3 m in S4. Thus, if we use the resistivity measured below 1.3 m deep as the saturated soils, we can estimate the volumetric water content based on Equation (5) for the active layer. We can first correct the temperature effect according to Equation (6) and then estimate the water content from Equation (2) by assuming homogeneous soil. Since the water content (θ) is equal to the average porosity (ϕ) in the unfrozen saturated zone, we have:

$$\rho_s = \alpha \rho_w \theta^{-2} = \alpha \rho_w \phi^{-2}, \tag{4}$$

Because the tortuosity factor (α) and the resistivity of the pore water (ρ_w) is observed in same tomogram and area, those parameters have the same value. The volumetric water content in the active layer can be estimated as:

$$\theta = \phi \sqrt{\frac{\rho_s}{\rho_u}} \tag{5}$$

Additionally, resistivity is affected by the decrease in rock temperatures above the freezing point. Keller and Frischknecht [33] derived the relationships between resistivity (ρ_t) and the temperature difference ($T - T_0$) from the resistivity value (ρ_0) at a reference temperature (T_0):

$$\rho_t = \frac{\rho_0}{1 + \alpha (T - T_0)} \tag{6}$$

Here, the constant α approaches values of 0.025 K^{-1} for most electrolytes [33]. Hence, by correcting the temperature effect using Equation (6) and assuming that the average porosity of the washout is similar to that of the fluvial gravels (approximately 0.26), we should be able to estimate the water content in the active layer above the permafrost based on Equation (5). Figure 10 presents the estimated water content in the active layer above the permafrost in the monitoring well.

Further determination of hydraulic parameters and groundwater table within the Soil Water Characteristic Curve (SWCC) from the Van Genuchten model [34] can be achieved utilizing the methodologies delineated by Lin et al. [25,26]. The Van Genuchten model can be described as:

$$\theta(h) = \theta_r + \frac{\theta_s - \theta_r}{\left[1 + (\alpha h)^n\right]^m}, \tag{7}$$

where $\theta(h)$ represents the normalized water content, α is related to the inverse of air entry value, where θ_r is the residual water content, θ_s is the saturated water content, h is the

suction head, n is related to the pore size distribution of the soil, m is associated with the asymmetry of the model, and m is equal to $1 - n^{-1}$.

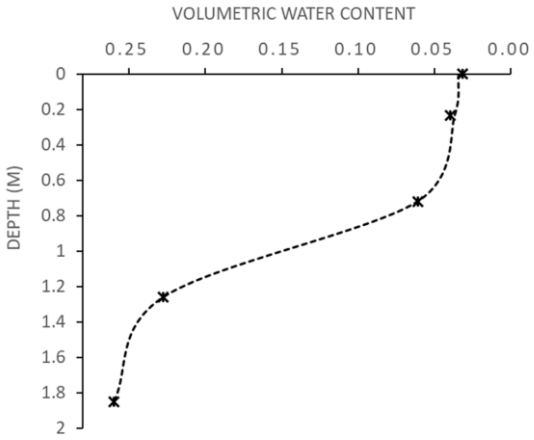

Figure 10. The estimated water content (cross mark) and fitted water content distribution (dashed line) in the temperature monitoring well on the ST line.

The parameters were derived through fitting the water content to the SWCC of the Van Genuchten model, aiming to minimize the root mean square discrepancies between predicted and observed water content values. The measured water content was obtained through resistivity measurements. Therefore, we were able to estimate the depth of the groundwater table without using pressure sensors but estimate the depth of groundwater with the air-entry suction head (h_a), and the depth where water content was in a saturated condition ($\theta = \theta_s$), as described by Chang, et al. [35] and Puntu et al. [26]:

$$D_{GW} = D_s - h_a, \tag{8}$$

where D_{GW} is the groundwater depth; D_s is the depth of the saturated layer.

The estimated depth of the groundwater table for the position of temperature monitoring well on the ST line was approximately 1.06 m and the estimated relative parameters of the SWCC curve were shown in Table 3. This estimation closely aligns with the groundwater table measured in the S4 borehole (about 1.30 m deep), given that the ground surface at the monitoring well was about 20 cm higher than that of S4.

Table 3. The estimated relative parameters of the SWCC curve.

θ_s	θ_s	n	m	α	D_s (m)	h_a (m)	D_{GW} (m)
0.26	0.03	6.11	0.84	0.77	1.30	0.24	1.06

5. Conclusions

In the study, we conducted electrical resistivity imaging (ERI) measurements near the Nicolaus Copernicus University Polar Station (NCUPS), located on the western coast of Spitsbergen on the Svalbard archipelago. Along the 148-m-long LN survey line, approximately perpendicular to the coastline, we conducted ERI surveys in August 2022 and 2023. Additionally, we performed ERI surveys along the 40-m-long ST line to compare measured resistivity with subsurface temperatures.

Overall, the LN resistivity profile in 2022 and 2023 exhibited a similar distribution pattern. However, the difference of the inverted resistivity images between 2022 and 2023 revealed a decrease in resistivity by about 600 Ohm.m in the unsaturated active layer, except for some regions rich in remaining ice. Considering the temperature increased by 5.8 °C with no significant precipitation variation in 2023 compared to 2022, we attribute the decreased resistivity to the temperature increase, possibly caused by global climate change.

The ST line shows that the resistivity reached its lowest point at a depth of approximately 1.6 m, then increased to over 200 Ohm.m at around 4 m, and slightly decreased to approximately 150 Ohm.m at a depth of 7 m. Temperature measurements collected from the monitoring well along the ST line confirmed that the active layer extended to around 1.6 m, with permafrost located at greater depths.

Additionally, we attempted to estimate the water content distribution and groundwater table in the ST line by using the Soil Water Characteristic Curve from the Van Genuchten model. The results showed that the estimated groundwater depth was located at about 1.06 m deep, consistent with the measured groundwater table in the S4 borehole on the ST line.

Furthermore, this study presented an advance understanding of permafrost behavior in the Arctic, and provides insight into the sensitivity of resistivity patterns to climate change, providing substantial information on subsurface dynamics in the region.

Author Contributions: Conceptualization, D.-J.L., P.-Y.C., Y.-L.C. and C.-F.N.; data curation, D.-J.L., P.-Y.C., J.M.P., C.-F.N., K.C. and Y.-H.C.; formal analysis, D.-J.L., P.-Y.C., Y.-L.C. and J.M.P.; funding acquisition, P.-Y.C., C.-F.N. and S.J.G.; investigation, D.-J.L., P.-Y.C., Y.-L.C., C.-F.N., S.J.G., K.C. and Y.-H.C.; methodology, D.-J.L., P.-Y.C., Y.-L.C. and J.M.P.; project administration, P.-Y.C., C.-F.N., S.J.G. and I.S.; resources, P.-Y.C., C.-F.N., S.J.G. and I.S.; visualization, D.-J.L., Y.-L.C., J.M.P. and S.J.G.; writing—original draft, D.-J.L. and P.-Y.C.; writing—review and editing, D.-J.L., P.-Y.C., S.J.G. and I.S. All authors have read and agreed to the published version of the manuscript.

Funding: This research supported by the National Academy of Marine Research, Taiwan, Ministry 355 of Foreign Affairs, R.O.C. (Taiwan) and National Central University, Taiwan.

Data Availability Statement: The datasets used and/or analyzed during the current study are available from the corresponding author on reasonable request.

Acknowledgments: The author thanks the Ministry of Education, Taiwan, the Ministry of Foreign Affairs, Taiwan, the National Central University (NCU), and the National Academy of Marine Research (NAMR), Taiwan, for supporting the research. The author also thanks the Nicholas Copernicus University Polar Station and the Taiwan Polar Institute for supporting the in situ survey and monitoring. This study is partly supported by the CRIOS project (Cryosphere Integrated Observatory Network on Svalbard). The CRIOS project is generously funded by the EEA funding scheme for basic research.

Conflicts of Interest: The authors declare no conflicts of interest.

References

1. ACGR. *Glossary of Permafrost and Related Ground-Ice Terms*; Technical Memorandum No. 142; Associate Committee on Geotechnical Research, Permafrost Subcommittee, National Research Council of Canada: Ottawa, ON, Canada, 1988; p. 155.
2. Rossi, M.; Dal Cin, M.; Picotti, S.; Gei, D.; Isaev, V.S.; Pogorelov, A.V.; Gorshkov, E.I.; Sergeev, D.O.; Kotov, P.I.; Giorgi, M.; et al. Active Layer and Permafrost Investigations Using Geophysical and Geocryological Methods—A Case Study of the Khanovey Area, Near Vorkuta, in the NE European Russian Arctic. *Front. Earth Sci.* **2022**, *10*, 1–22. [CrossRef]
3. Zhang, T.; Barry, R.; Knowles, K.; Heginbottom, J.; Brown, J. Statistics and characteristics of permafrost and ground-ice distribution in the Northern Hemisphere. *Polar Geogr.* **2008**, *31*, 47–68. [CrossRef]
4. Gruber, S. Derivation and analysis of a high-resolution estimate of global permafrost zonation. *Cryosphere* **2012**, *6*, 221–233. [CrossRef]
5. Wang, C.; Wang, Z.; Kong, Y.; Zhang, F.; Yang, K.; Zhang, T. Most of the northern hemisphere permafrost remains under climate change. *Sci. Rep.* **2019**, *9*, 3295. [CrossRef] [PubMed]
6. Harris, S.A.; Brouchkov, A.; Guodong, C. *Geocryology: Characteristics and Use of Frozen Ground and Permafrost Landforms*; CRC Press: Boca Raton, FL, USA, 2017.
7. IPCC. *Meeting Report of the Intergovernmental Panel on Climate Change Expert Meeting on Mitigation, Sustainability and Climate Stabilization Scenarios*; IPCC: Geneva, Switzerland, 2017.
8. Biskaborn, B.K.; Smith, S.L.; Noetzli, J.; Matthes, H.; Vieira, G.; Streletskiy, D.A.; Schoeneich, P.; Romanovsky, V.E.; Lewkowicz, A.G.; Abramov, A. Permafrost is warming at a global scale. *Nat. Commun.* **2019**, *10*, 264. [CrossRef]
9. NSIDC. Advancing Knowledge of Earth's Frozen Regions. Cryosphere Glossary. Available online: https://nsidc.org/cryosphere/glossary (accessed on 15 July 2024).
10. Chen, T.; Ma, W.; Wu, Z.-J.; Mu, Y.-H. Characteristics of dynamic response of the active layer beneath embankment in permafrost regions along the Qinghai–Tibet Railroad. *Cold Reg. Sci. Technol.* **2014**, *98*, 1–7. [CrossRef]

11. Isaksen, K.; Sollid, J.L.; Holmlund, P.; Harris, C. Recent warming of mountain permafrost in Svalbard and Scandinavia. *J. Geophys. Res. Earth Surf.* **2007**, *112*, 1–11. [CrossRef]
12. Sobota, I.; Nowak, M. Changes in the dynamics and thermal regime of the permafrost and active layer of the high arctic coastal area in north-west spitsbergen, svalbard. *Geogr. Ann. Ser. A Phys. Geogr.* **2014**, *96*, 227–240. [CrossRef]
13. Sobota, I.; Weckwerth, P.; Grajewski, T.; Dziembowski, M.; Greń, K.; Nowak, M. Short-term changes in thickness and temperature of the active layer in summer in the Kaffiøyra region, NW Spitsbergen, Svalbard. *Catena* **2018**, *160*, 141–153. [CrossRef]
14. Keating, K.; Binley, A.; Bense, V.; Van Dam, R.L.; Christiansen, H.H. Combined geophysical measurements provide evidence for unfrozen water in permafrost in the Adventdalen valley in Svalbard. *Geophys. Res. Lett.* **2018**, *45*, 7606–7614. [CrossRef]
15. Rouyet, L.; Lauknes, T.R.; Christiansen, H.H.; Strand, S.M.; Larsen, Y. Seasonal dynamics of a permafrost landscape, Adventdalen, Svalbard, investigated by InSAR. *Remote Sens. Environ.* **2019**, *231*, 111236. [CrossRef]
16. Hinkel, K.; Doolittle, J.; Bockheim, J.; Nelson, F.; Paetzold, R.; Kimble, J.M.; Travis, R. Detection of subsurface permafrost features with ground-penetrating radar, Barrow, Alaska. *Permafr. Periglac. Process.* **2001**, *12*, 179–190. [CrossRef]
17. Kim, K.; Lee, J.; Ju, H.; Jung, J.Y.; Chae, N.; Chi, J.; Kwon, M.J.; Lee, B.Y.; Wagner, J.; Kim, J.-S. Time-lapse electrical resistivity tomography and ground penetrating radar mapping of the active layer of permafrost across a snow fence in Cambridge Bay, Nunavut Territory, Canada: Correlation interpretation using vegetation and meteorological data. *Geosci. J.* **2021**, *25*, 877–890. [CrossRef]
18. Forte, E.; French, H.M.; Raffi, R.; Santin, I.; Guglielmin, M. Investigations of polygonal patterned ground in continuous Antarctic permafrost by means of ground penetrating radar and electrical resistivity tomography: Some unexpected correlations. *Permafr. Periglac. Process.* **2022**, *33*, 226–240. [CrossRef]
19. Sobota, I. *Współczesne Zmiany Kriosfery Północno-Zachodniego Spitsbergenu na Przykładzie Regionu Kaffiøyry*; Wydawnictwo Naukowe Uniwersytetu Mikołaja Kopernika: Toruń, Poland, 2013.
20. Sobota, I.; Nowak, M.; Weckwerth, P. Long-term changes of glaciers in north-western Spitsbergen. *Glob. Planet. Change* **2016**, *144*, 182–197. [CrossRef]
21. Schuler, T.V.; Kohler, J.; Elagina, N.; Hagen, J.O.M.; Hodson, A.J.; Jania, J.A.; Kääb, A.M.; Luks, B.; Małecki, J.; Moholdt, G. Reconciling Svalbard glacier mass balance. *Front. Earth Sci.* **2020**, *8*, 156. [CrossRef]
22. Kejna, M.; Sobota, I. Meteorological conditions on Kaffiøyra (NW Spitsbergen) in 2013–2017 and their connection with atmospheric circulation and sea ice extent. *Pol. Polar Res.* **2019**, *40*, 175–204. [CrossRef]
23. Lippmann, E. *4-Point Light hp Technical Data and Operating Instructions*; Version 3.37; Geophysikalische Messgerate: Schaufling, Germany, 2005; Volume 28.
24. Dahlin, T.; Zhou, B. A numerical comparison of 2D resistivity imaging with 10 electrode arrays. *Geophys. Prospect.* **2004**, *52*, 379–398. [CrossRef]
25. Lin, D.-J.; Chang, P.-Y.; Puntu, J.M.; Doyoro, Y.G.; Amania, H.H.; Chang, L.-C. Estimating the specific yield and groundwater level of an unconfined aquifer using time-lapse electrical resistivity imaging in the pingtung plain, Taiwan. *Water* **2023**, *15*, 1184. [CrossRef]
26. Puntu, J.M.; Chang, P.-Y.; Amania, H.H.; Lin, D.-J.; Sung, C.-Y.; Suryantara, M.; Chang, L.-C.; Doyoro, Y.G. Groundwater monitoring and specific yield estimation using time-lapse electrical resistivity imaging and machine learning. *Front. Environ. Sci.* **2023**, *11*, 1197888. [CrossRef]
27. AGI. *Instruction Manual for EarthImager 2D 2.3.0*; AGI: Virginia Beach, VA, USA, 2006; Volume 62.
28. Yang, X.; Lagmanson, M.B. Planning resistivity surveys using numerical simulations. In Proceedings of the 16th EEGS Symposium on the Application of Geophysics to Engineering and Environmental Problems, San Antonio, TX, USA, 6–10 April 2003; p. cp-190-00047.
29. Sharma, S.; Verma, G.K. Inversion of electrical resistivity data: A review. *Int. J. Comput. Syst. Eng.* **2015**, *9*, 400–406.
30. Archie, G.E. The electrical resistivity log as an aid in determining some reservoir characteristics. *Trans. AIME* **1942**, *146*, 54–62. [CrossRef]
31. Dakhnov, V.N.; Keller, G.V. *Geophysical Well Logging: The Application of Geophysical Methods*; Colorado School of Mines: Golden, CO, USA, 1962.
32. Glover, P.W. Archie's law—A reappraisal. *Solid Earth* **2016**, *7*, 1157–1169. [CrossRef]
33. Keller, G.V.; Frischknecht, F.C. *Electrical Methods in Geophysical Prospecting*; Pergamon: Oxford, UK, 1966.
34. Van Genuchten, M.T. A closed-form equation for predicting the hydraulic conductivity of unsaturated soils. *Soil Sci. Soc. Am. J.* **1980**, *44*, 892–898. [CrossRef]
35. Chang, P.-Y.; Puntu, J.M.; Lin, D.-J.; Yao, H.-J.; Chang, L.-C.; Chen, K.-H.; Lu, W.-J.; Lai, T.-H.; Doyoro, Y.G. Using Time-Lapse Resistivity Imaging Methods to Quantitatively Evaluate the Potential of Groundwater Reservoirs. *Water* **2022**, *14*, 420. [CrossRef]